INTERNATIONAL JOURNAL FOR NUMERICAL METHODS IN FLUIDS
Int. J. Numer. Meth. Fluids 2005; **48**:565–582
Published online 7 March 2005 in Wiley InterScience (www.interscience.wiley.com). DOI: 10.1002/fld.955

The advantages of using high-order finite differences schemes in laminar–turbulent transition studies

L. F. Souza[1,*,†], M. T. Mendonça[2] and M. A. F. Medeiros[3]

[1] *USP—Universidade de São Paulo, São Carlos ICMC-SCE, Av. Trabalhador São Carlense, 400 São Carlos, SP-13560-970, Brazil*
[2] *Centro Técnico Aeroespacial CTA-IAE-ASA-P, Pç Mal. Eduardo Gomes, 50 São José dos Campos, SP-12228 904, Brazil*
[3] *USP—Universidade de São Paulo, São Carlos EESC-SMM, Av. Trabalhador São Carlense, 400 São Carlos, SP-13566-590, Brazil*

SUMMARY

This paper presents various finite difference schemes and compare their ability to simulate instability waves in a given flow field. The governing equations for two-dimensional, incompressible flows were solved in vorticity–velocity formulation. Four different space discretization schemes were tested, namely, a second-order central differences, a fourth-order central differences, a fourth-order compact scheme and a sixth-order compact scheme. A classic fourth-order Runge–Kutta scheme was used in time. The influence of grid refinement in the streamwise and wall normal directions were evaluated. The results were compared with linear stability theory for the evolution of small-amplitude Tollmien–Schlichting waves in a plane Poiseuille flow. Both the amplification rate and the wavenumber were considered as verification parameters, showing the degree of dissipation and dispersion introduced by the different numerical schemes. The results confirmed that high-order schemes are necessary for studying hydrodynamic instability problems by direct numerical simulation. Copyright © 2005 John Wiley & Sons, Ltd.

KEY WORDS: high-order finite differences; compact difference schemes; vorticity–velocity formulation; hydrodynamic instability

1. INTRODUCTION

In many applications the ability to predict whether a given flow is laminar or turbulent is crucial, since heat transfer rates and skin friction coefficients are much larger in turbulent flows.

*Correspondence to: L. F. Souza, USP—Universidade de São Paulo, São Carlos ICMC-SCE, Av. Trabalhador São Carlense, 400 São Carlos, SP-13560-970, Brazil.
†E-mail: lefraso@icmc.usp.br

Contract/grant sponsor: FAPESP

Received 23 June 2003
Revised 27 August 2004
Accepted 31 January 2005

The knowledge of the flow regime whether, laminar, transitional or turbulent, is necessary for the correct design of aerodynamic surfaces or cooling systems. In certain situations it is even desirable to control the evolution of a laminar flow in order to delay transition and reduce viscous drag [1–3].

The direct numerical simulation (DNS) of the Navier–Stokes equations for studying stability and transition is becoming more feasible with the increasing capacity of modern computational resources. Different approaches have been presented in the literature [4–7] and a common factor among them is the use of high-resolution discretization methods [8]. This is because the numerical study of hydrodynamic stability and transition to turbulence requires the correct representation of a range of spatial and time scales. Spectral methods can be used to assure that all relevant scales are captured, but higher order finite differences are also able to represent short length scales with good accuracy. Lele [9] emphasizes the importance of using high-order methods for these flows and shows schemes for first and second derivatives of second to tenth order. Mahesh [10] shows higher order finite difference schemes, and a scheme that is more accurate than the standard Padé schemes using the same stencil. The disadvantage of this method is that it requires the solution of first and second derivatives simultaneously. Hirsh [11] and Adam [12] also discuss some advantages of a fourth-order compact method compared to standard methods.

Another relevant aspect to be considered in direct numerical simulation of stability and transition problems is grid refinement. Coarse-grid simulations can result in artificial dissipation.

In the current study, a formulation based on the vorticity–velocity variables [13–17] was adopted. The growth of instability modes in a two-dimensional Poiseuille incompressible flow was simulated. The disturbances introduced in the flow field can grow, decay or stay constant depending on the Reynolds number and frequency.

The emphasis in this paper is on inferring what degree of resolution is needed to capture reliably the instantaneous structure of a disturbed flow. Only the linear propagation of the disturbances were analysed, since the exact solution from linear stability theory is available. In Section 2, the governing equations are derived, and the details of the numerical methods are described. The time and spatial discretization used are also shown in this section. The four different schemes used to discretize spatial derivatives are presented, namely, second-order explicit central difference schemes, fourth-order explicit central difference schemes, fourth-order implicit (compact) central difference schemes and sixth-order implicit (compact) central difference schemes. Section 3 presents details of the linear stability analysis for plane Poiseuille flows. In Section 4, the results of the propagation of a stable, a neutral and an unstable disturbances using a sixth-order compact method are given. Then, simulations using the other three approaches for spatial derivatives are also presented for a neutral disturbance. Section 5 presents the conclusions and final comments.

2. FORMULATION AND NUMERICAL METHOD

For the numerical solution, the Navier–Stokes equations were written in the vorticity–velocity formulation. The vorticity in the spanwise direction, denoted by ω_z, is

$$\omega_z = \frac{\partial u}{\partial y} - \frac{\partial v}{\partial x} \tag{1}$$

In two-dimension, the vorticity transport equation is given by

$$\frac{\partial \omega_z}{\partial t} + u\frac{\partial \omega_z}{\partial x} + v\frac{\partial \omega_z}{\partial y} = \frac{1}{Re}\left(\frac{\partial^2 \omega_z}{\partial x^2} + \frac{\partial^2 \omega_z}{\partial y^2}\right) \tag{2}$$

while the continuity equation is

$$\frac{\partial u}{\partial x} + \frac{\partial v}{\partial y} = 0 \tag{3}$$

From the vorticity equation (1) and the continuity equation (3) a Poisson-type equation for the v velocity component can be derived:

$$\frac{\partial^2 v}{\partial x^2} + \frac{\partial^2 v}{\partial y^2} = -\frac{\partial \omega_z}{\partial x} \tag{4}$$

Equations (2)–(4) were solved numerically and the solution was marched in time according to the following steps:

(i) Impose initial conditions for u, v and ω_z compatible with each other.
(ii) Introduce disturbances at the inlet boundary, using eigenfunctions obtained from solving the Orr–Sommerfeld equation for the Poiseuille flow.
(iii) Calculate the vorticity from the vorticity transport equation (2), at time $t + \mathrm{d}t$.
(iv) Calculate the v velocity component from the Poisson equation (4).
(v) Calculate the u velocity component from the continuity equation (3).
(vi) Calculate the vorticity generation at the wall for the velocity distribution at $t + \mathrm{d}t$, using Equation (4) and taking into account that $\partial^2 v/\partial x^2 = 0$.
(vii) Return to the second step (ii) until the desired integration time was reached.

The time derivative in the vorticity transport equation was discretized with a classical fourth-order Runge–Kutta integration scheme [18]. For each intermediate step in the Runge–Kutta integration it was necessary to update the velocity field and the vorticity at the wall by taking steps (iv)–(vi) in the steps described above.

For the spatial derivatives four different schemes were used. The discretization used for each method is presented below, taking the derivatives in x direction as an example, since it was analogous to the y derivatives. The letter i represents the grid position in the x direction, which varies from 1 to N.

2.1. Second-order difference schemes

For $1 < i < N$:

$$f'_i = \frac{f_{i+1} - f_{i-1}}{2\,\mathrm{d}x} + O(\mathrm{d}x^2) \tag{5}$$

$$f''_i = \frac{f_{i+1} - 2f_i + f_{i-1}}{\mathrm{d}x^2} + O(\mathrm{d}x^2) \tag{6}$$

For $i = 1$:

$$f'_1 = \frac{-3f_1 + 4f_2 - f_3}{2\,\mathrm{d}x} + O(\mathrm{d}x^2) \tag{7}$$

$$f_1'' = \frac{6f_1 - 15f_2 + 12f_3 - 3f_4}{\mathrm{d}x^2} + O(\mathrm{d}x^2) \tag{8}$$

For $i = N$:

$$f_N' = \frac{3f_N - 4f_{N-1} + f_{N-2}}{2\,\mathrm{d}x} + O(\mathrm{d}x^2) \tag{9}$$

$$f_N'' = \frac{6f_N - 15f_{N-1} + 12f_{N-2} - 3f_{N-3}}{\mathrm{d}x^2} + O(\mathrm{d}x^2) \tag{10}$$

2.2. Fourth-order explicit difference schemes

For $2 < i < N - 1$:

$$f_i' = \frac{f_{i-2} - 8f_{i-1} + 8f_{i+1} - f_{i+2}}{12\,\mathrm{d}x} + O(\mathrm{d}x^4) \tag{11}$$

$$f_i'' = \frac{-f_{i-2} + 16f_{i-1} - 30f_i + 16f_{i+1} - f_{i+2}}{12\,\mathrm{d}x^2} + O(\mathrm{d}x^4) \tag{12}$$

For $i = 1$:

$$f_1' = \frac{-50f_1 + 96f_2 - 72f_3 + 32f_4 - 6f_5}{24\,\mathrm{d}x} + O(\mathrm{d}x^4) \tag{13}$$

$$f_1'' = \frac{225f_1 - 770f_2 + 1070f_3 - 780f_4 + 305f_5 - 50f_6}{60\,\mathrm{d}x^2} + O(\mathrm{d}x^4) \tag{14}$$

For $i = 2$:

$$f_2' = \frac{-6f_1 - 20f_2 + 36f_3 - 12f_4 + 2f_5}{24\,\mathrm{d}x} + O(\mathrm{d}x^4) \tag{15}$$

$$f_2'' = \frac{50f_1 - 75f_2 - 20f_3 + 70f_4 - 30f_5 + 5f_6}{60\,\mathrm{d}x^2} + O(\mathrm{d}x^4) \tag{16}$$

$$f_2'' = \frac{11f_1 - 20f_2 + 6f_3 + 4f_4 - f_5}{12\,\mathrm{d}x^2} + O(\mathrm{d}x^3) \tag{17}$$

The use of a fourth- and third-order approximations for $i = 2$ and $N - 1$ is discussed in the section considering the numerical results. The approximations for $i = N$ and $N - 1$ were analogous to the approximations for $i = 1$ and 2, the only modification was in the sign of the first derivative, as one can observe in the approximations of second-order accuracy.

2.3. Fourth-order compact difference schemes

In this scheme, to find the values of the derivatives a matrix must be solved, where all the derivatives in a grid line are treated simultaneously.

For the first derivative, at the boundary, $i=1$:

$$f'_1 + 3f'_2 = \frac{1}{6\,\mathrm{d}x}(-17f_1 + 9f_2 + 9f_3 - f_4) + O(\mathrm{d}x^3) \tag{18}$$

For the interior points, the following approximation was used:

$$f'_{i-1} + 4f'_i + f'_{i+1} = \frac{3}{\mathrm{d}x}(-f_{i-1} + f_{i+1}) + O(\mathrm{d}x^4) \tag{19}$$

For the second derivatives, at the boundary, $i=1$, the approximation adopted was

$$f''_1 + 11f''_2 = \frac{1}{3\,\mathrm{d}x^2}(39f_1 - 81f_2 + 45f_3 - 3f_4) + O(\mathrm{d}x^3) \tag{20}$$

For the interior points, the following approximation was used:

$$f''_{i-1} + 10f''_i + f''_{i+1} = \frac{12}{\mathrm{d}x^2}(f_{i-1} - 2f_i + f_{i+1}) + O(\mathrm{d}x^4) \tag{21}$$

2.4. Sixth-order compact difference schemes

The sixth-order compact approximations proposed here differ from the approximations given by Lele [9] in the discretization of the boundary and near-boundary points. At the boundaries, a third-order approximation is used by Lele, whereas for points next to the boundaries he used a fourth-order approximation. In the current work the use of a greater order approximations at these boundaries was necessary. Therefore, a fifth-order approximation was used for the boundary points. For points next to the boundaries, a sixth-order approximation was used.

The details of the discretization scheme were as follows. For the first derivative, at the boundary, $i=1$:

$$f'_1 + 4f'_2 = \frac{1}{24\,\mathrm{d}x}(-74f_1 + 16f_2 + 72f_3 - 16f_4 + 2f_5) + O(\mathrm{d}x^5) \tag{22}$$

For the points next to the boundary, $i=2$:

$$f'_1 + 6f'_2 + 2f'_3 = \frac{1}{120\,\mathrm{d}x}(-406f_1 - 300f_2 + 760f_3 - 80f_4 + 30f_5 - 4f_6) + O(\mathrm{d}x^6) \tag{23}$$

For the points at the opposite boundary, $i=N$ and $N-1$, similar approximations were used. For the interior points, a sixth-order Padé approximation was used:

$$f'_{i-1} + 3f'_i + f'_{i+1} = \frac{1}{12\,\mathrm{d}x}(-f_{i-2} - 28f_{i-1} + 28f_{i+1} + f_{i+2}) + O(\mathrm{d}x^6) \tag{24}$$

The second derivatives, at the boundary, $i=1$, were discretized using a fifth-order asymmetric approximation:

$$13f''_1 + 137f''_2 = \frac{1}{120\,\mathrm{d}x^2}(9775f_1 - 20285f_2 + 11170f_3 - 550f_4 - 145f_5 + 36f_6) + O(\mathrm{d}x^5) \tag{25}$$

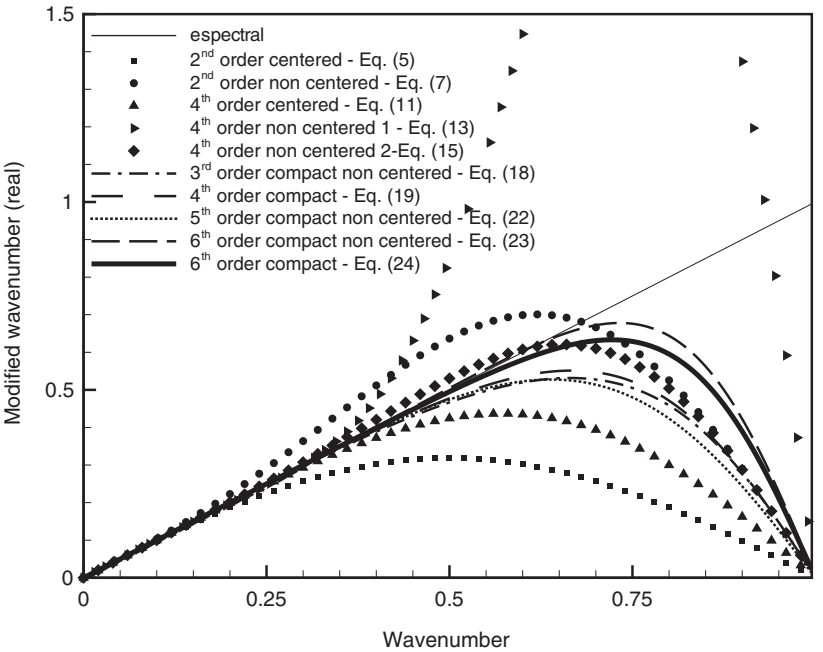

Figure 1. Modified wavenumber vs wavenumber for first derivative approximations—real part.

For the points near the boundary, $i=2$, a sixth-order asymmetric approximation was used:

$$f_1'' + 12f_2'' + 3f_3'' = \frac{1}{360\,\mathrm{d}x^2}(4834f_1 - 8424f_2 + 1890f_3 + 2320f_4 - 810f_5 + 216f_6 - 26f_7) + O(\mathrm{d}x^6) \tag{26}$$

For the interior points a sixth-order Padé approximation was used:

$$2f_{i-1}'' + 11f_i'' + 2f_{i+1}'' = \frac{1}{4\,\mathrm{d}x^2}(3f_{i-2} + 48f_{i-1} - 102f_i + 48f_{i+1} + 3f_{i+2}) + O(\mathrm{d}x^6) \tag{27}$$

For the points at the opposite boundary, $i=N$ and $N-1$, similar approximations to the ones used for points $i=1$ and 2 were used.

A Fourier analysis of the finite difference schemes were performed and the results are shown in Figures 1–4. Plots of the real part of the modified wavenumber of the finite difference schemes against the wavenumber for the first derivative calculation are presented in Figure 1. In this figure the resolution characteristics of the different schemes can be compared. The wavenumber was normalized by $k_{\max} = \pi/\Delta x$. According to Reference [9], the difference between the modified wavenumber and the exact (spectral) value can be associated with a dispersion error. In Figures 1–4, the wavenumber is related to the number of points (N) per wavelength by $k = 1/((N-1)/2)$. In Figure 2, the imaginary part of the modified wavenumber of the finite difference schemes against the wavenumber of the finite difference schemes for the first derivative calculation is shown. The exact result should be zero for all wavenumbers,

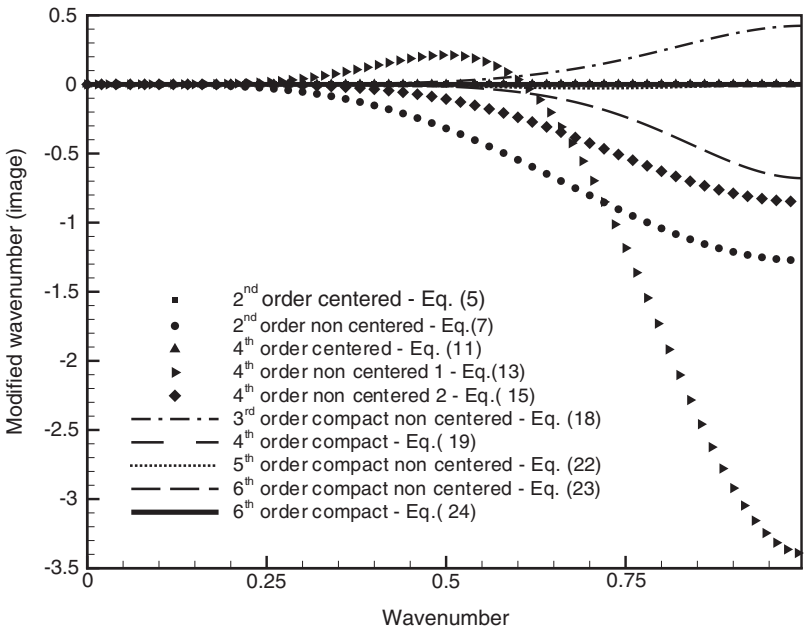

Figure 2. Modified wavenumber vs wavenumber for first derivative approximations—imaginary part.

and the difference can be associated with a dissipation of the numerical scheme [9]. The real and the imaginary parts of the modified wavenumber of the finite difference schemes for the second derivative calculation is shown in Figures 3 and 4. In this analysis, it can be observed that the sixth-order compact scheme gives the best result for both first and second derivative calculations.

To solve the Poisson equation, a line successive over-relaxation (LSOR) method was used. The method was a combination of a fourth-order explicit approximation in the x direction and a sixth-order compact approximation in the y direction. Some tests were made using a full sixth-order compact approximation method and no relevant differences in the results were found. The full sixth-order compact method required a larger computational effort, therefore, in these simulations, the combination method was adopted.

Three types of boundary conditions are needed to be specified: inflow boundary condition, wall boundary condition and outflow boundary condition.

At the inlet, the boundary condition was specified by superposing a small disturbance onto the laminar Poiseuille flow velocity $U(y)$ and vorticity $\Omega_z(y)$ distributions:

$$\begin{aligned} u(x_0, y, t) &= U(y) + u'(x_0, y, t) \\ v(x_0, y, t) &= v'(x_0, y, t) \\ \omega_z(x_0, y, t) &= \Omega_z(y) + \omega'_z(x_0, y, t) \end{aligned} \tag{28}$$

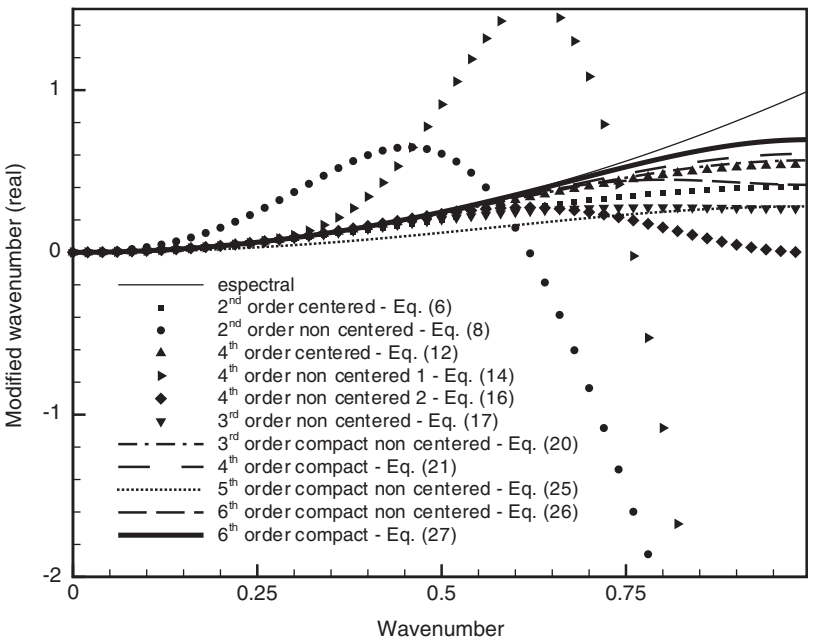

Figure 3. Differencing error for second derivative approximations vs wavenumber—real part.

The slope of the small disturbance was given by the solution of a linear stability analysis. The Orr–Sommerfeld equation was solved and the disturbances were built from the resulting eigenfunctions and eigenvalues.

At the wall, no-slip boundary conditions were imposed:

$$u = v = 0 \tag{29}$$

As adopted by Fasel [19], the vorticity at the wall was calculated from the Poisson equation. Equation (4), applied at the wall, where the second derivative of u vanishes, gives:

$$\frac{\partial \omega_z}{\partial x} = -\frac{\partial^2 v}{\partial y^2} \tag{30}$$

This equation was discretized using, for the second derivative in the normal direction:

$$\frac{\partial^2 v}{\partial y^2} = -\frac{216v_{i,j+1} - 135v_{i,j+2} + 80v_{i,j+3} - 33.75v_{i,j+4} + 8.64v_{i,j+5} - v_{i,j+6}}{18\Delta y^2} \tag{31}$$

and the vorticity was calculated with the approximation:

$$\omega_{i,1} = \frac{\Delta x}{57}\left[10\left.\frac{\partial^2 v}{\partial y^2}\right|_{i-2,1} + 57\left.\frac{\partial^2 v}{\partial y^2}\right|_{i-1,1} + 24\left.\frac{\partial^2 v}{\partial y^2}\right|_{i,1} - \left.\frac{\partial^2 v}{\partial y^2}\right|_{i+1,1} + 33\omega_{i-2,1} + 24\omega_{i-1,1}\right] \tag{32}$$

These approximations take into account that $\partial v/\partial y = 0$ at the wall, ensuring divergence-free velocity field at this boundary.

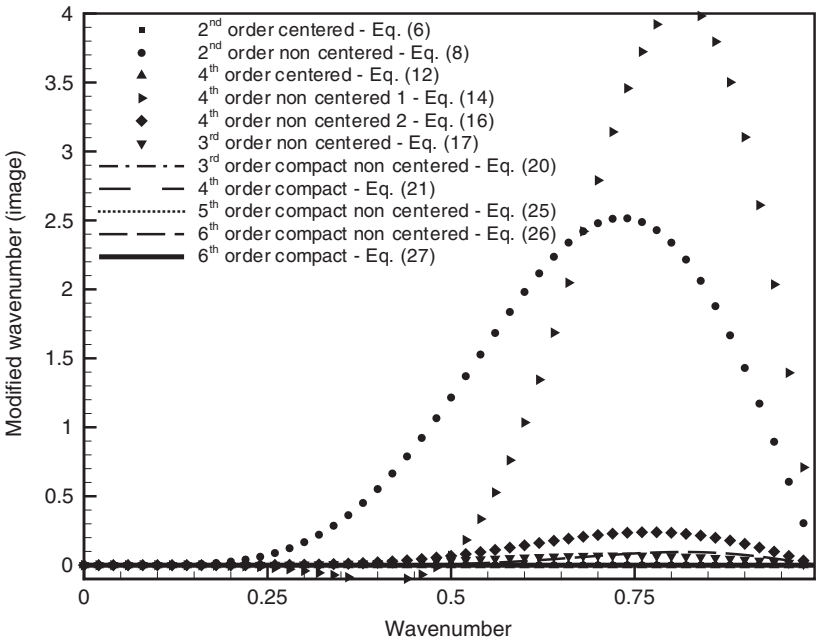

Figure 4. Differencing error for second derivative approximations vs wavenumber—imaginary part.

At the outflow boundary, the following condition was used:

$$\frac{\partial^2 v(X, y, t)}{\partial x^2} = -\alpha_r^2 v'(X, y, t) \tag{33}$$

where the term v' is the disturbance normal velocity component (Equation (34)) and X stands for the last point in the x direction. This condition was used in the Poisson equation (4), where the $v(X, y, t)$ velocity component is computed. The u velocity component was computed using the continuity equation, and the ω_z was obtained directly from the integration of the vorticity transport equation.

The boundary condition given by Equation (33) corresponds to the second derivative of an oscillatory disturbance with streamwise wavenumber α_r at a given time t. This allows the disturbances to pass through this boundary without reflections. The streamwise wavenumber is given by the linear stability solution for the considered frequency and Reynolds number.

3. LINEAR STABILITY THEORY

In order to test the numerical method described above, results for plane Poiseuille flow perturbed by small amplitude periodic disturbances were compared with linear stability theory results. The problem is illustrated schematically in Figure 5. The characteristic length scale L was half the channel height H, and the characteristic velocity scale was $U(y = H)$.

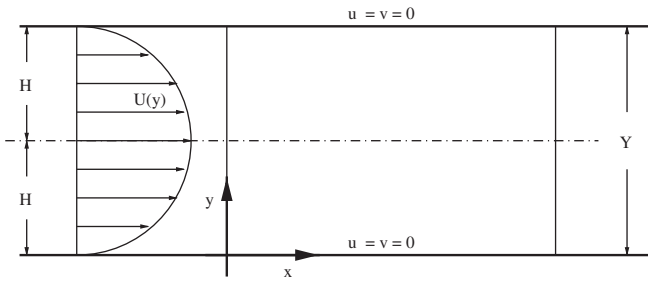

Figure 5. Schematic illustration of the domain and coordinate system for Poiseuille flow stability numerical simulation.

The linear stability theory assumes that the disturbances propagate in the flow as wave structures and gives a relationship between wavenumber α_r, frequency ω_t, wave speed $c = \omega_t/\alpha_r$ and growth rate α_i, such that:

$$v'(x, y, t) = \hat{v}(y)\mathrm{e}^{\mathrm{i}(\alpha_r x + \mathrm{i}\alpha_i) - \mathrm{i}\omega_t t} \tag{34}$$

where $v'(x, y, t)$ represents the wall normal component of velocity and $\hat{v}(y)$ is the complex amplitude distribution. The vorticity disturbance is represented likewise. The Navier–Stokes equations are simplified assuming that the instantaneous velocity can be decomposed into a parallel mean components $U(y)$ and an infinitesimal disturbance. The resulting equation is the Orr–Sommerfeld equation:

$$\alpha(U - c)(v'' - \alpha^2 v) - U''\alpha v = -\frac{\mathrm{i}}{Re}(v^{\mathrm{IV}} - 2\alpha^2 v'' + \alpha^4 v) \tag{35}$$

The Orr–Sommerfeld equation is an eigenvalue problem which leads to the stability diagram presented in Figure 6. This eigenvalue problem is solved using a shooting method [20]. The neutral curve, $\alpha_i = 0$ separates the unstable region ($\alpha_i < 0$) from the stable region ($\alpha_i > 0$).

In the present formulation the disturbances grow or decay in the downstream direction. The temporal analysis, where the disturbances grow or decay in time, is much less computationally intensive, but the spatial approach adopted in the present work was more consistent with the flow physics.

Three different test cases were considered, namely, an asymptotically stable case, a nearly neutrally stable case and an asymptotically unstable case, these cases are indicated in Figure 6 by points 'A', 'B' and 'C', respectively. The growth rates, wavenumbers and frequencies for these three cases are presented in Table I. The case 'B' is hereafter referred to as neutral case, although it is asymptotically stable with a very small growth rate, as one can observe in Table I.

In order to carry out the numerical experiments, the laminar Poiseuille flow velocity distribution was perturbed at the inlet boundary. The disturbance initial amplitude was equal to 5×10^{-4}. The spatial evolution of these disturbance were compared to the corresponding linear stability results at various downstream positions. The results are presented in the next section.

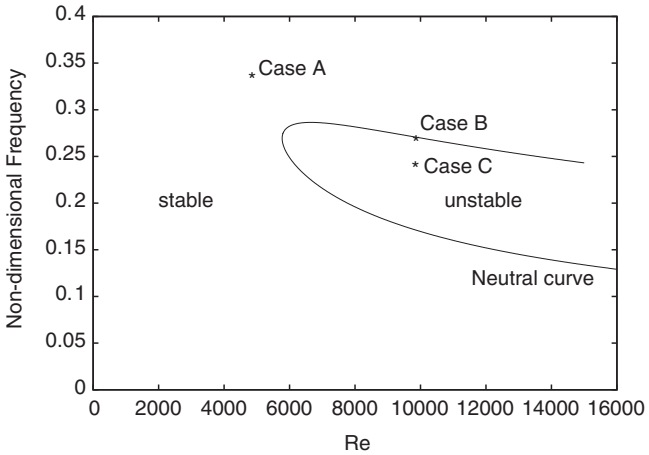

Figure 6. Neutral curve for Poiseuille flow.

Table I. Eigenvalues for the test cases.

	A	B	C
Re	5000	10000	10000
α_r	1.157	1.095	1.000
α_i	0.010	9.88×10^{-5}	-0.010
ω_t	0.330	0.270	0.2375

4. NUMERICAL RESULTS

To carry out the numerical experiments, a rectangular domain extending over 16 Tollmien–Schlichting wavelengths in the streamwise direction was set. In order to test the different spatial discretization methods, the number of grid points taken per Tollmien–Schlichting wavelength and the number of points in the wall normal direction were different for each simulation. The number of grid points per Tollmien–Schlichting wavelength tested were $6, 8, 12, 16$ and 32. In the wall normal direction $65, 81, 121, 161$ and 321 grid points were used. The number of time steps per wave-period used was 48, when using $6, 8$ or 12 grid points per wavelength, and 128, when using 16 or 32 grid points per Tollmien–Schlichting wavelength. The microcomputer used for all the simulations was an Atlon AMD 2000 XP.

4.1. Sixth-order compact approximation results

First the Poiseuille flow was simulated with the introduction of a stable, a neutral and an unstable disturbances using a sixth-order compact approximation for the spatial derivatives. Figure 7 shows a comparison between the numerical results and the LST results for the amplitude ratio (A/A_0) along the streamwise direction for a stable, a neutral and an unstable test case. In the figure, A stands for the amplitude of the disturbances, and A_0 is the amplitude

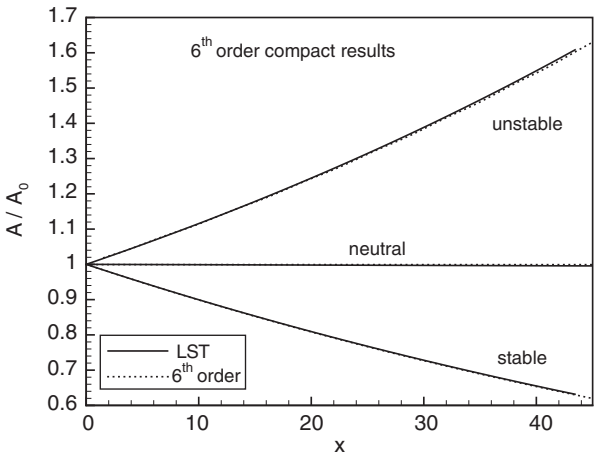

Figure 7. Sixth-order compact approximations—amplification results for the three test cases. Comparisons between numerical results (dots) and the LST results (lines).

imposed at $x = 0$. Several simulations with different number of grid points were performed. These simulations show that using the sixth-order compact approximations the results were accurate even with only 6 grid points per Tollmien–Schlichting wavelength and 65 grid points in the wall normal direction. The CPU time for this run was 41.89 s. Other simulations lowering the number of points in both direction were made, but the accuracy of the results reduced significantly.

Hereafter, the results are indicated by a label $N \times M$, where N is the number of points used per Tollmien–Schlichting wavelength and M is the number of points used in the wall normal direction. In Figure 8, for the neutral test case the phase distribution in the wall normal direction of the streamwise disturbance velocity component is plotted. This phase distribution was obtained by a temporal Fourier analysis of the disturbances. With this analysis one can obtain the real and the imaginary part of the wall normal disturbance velocity component v. The phase can be computed using the formula phase $= a\tan(v_i/v_r)$. The streamwise position adopted for the comparison of the results was $x = 45.89$. This streamwise position corresponds to half of channel length. The curves were plotted for half the channel height. The expected phase distribution, obtained with the LST is also plotted. The result obtained with the coarsest mesh (6×65) is still in good agreement with the LST. The phase plot gives quantitative information about the dispersion error.

For the next results, the test case used to compare the different spatial difference schemes and grid refinement was the neutral case (case 'B').

4.2. Second-order approximation results

The most refined grid mesh in this test had 32 points per Tollmien–Schlichting wavelength and 321 points in the wall normal direction. The total computing time for this simulation was 8301.8 s or 2 h 18 min and 21.8 s. In Figure 9, one can see that even by using this number of points the result obtained was not very accurate. In the same figure, results of three other

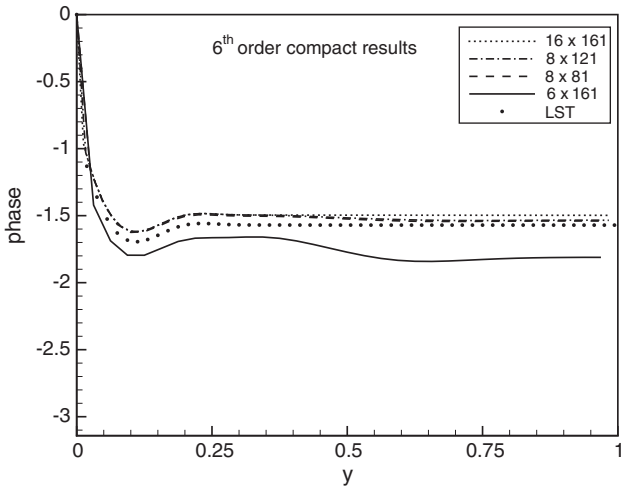

Figure 8. Phase results with different mesh sizes for sixth-order compact scheme at $x = 45.89$.

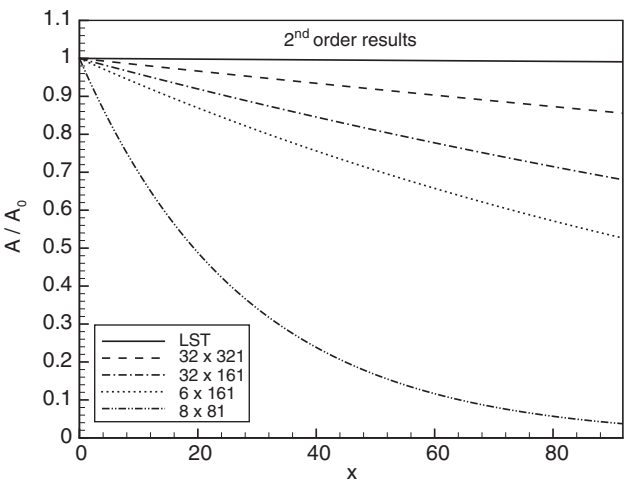

Figure 9. Second-order approximations—amplification results.

simulations using different mesh spacing are plotted. Lowering the number of grid points in any direction results in larger error.

Figure 10 shows the phase distribution plot for the second-order scheme. It shows that a large number of grid points were required to keep the dispersion within acceptable values.

The disturbance normal velocity component distribution along the streamwise direction at the centre of the channel ($y = H$) is plotted in Figure 11. The expected velocity distribution obtained with the LST is also plotted. This plot shows the effects of dispersion (phase speed error) and growth rate for the second-order scheme for different grid refinements.

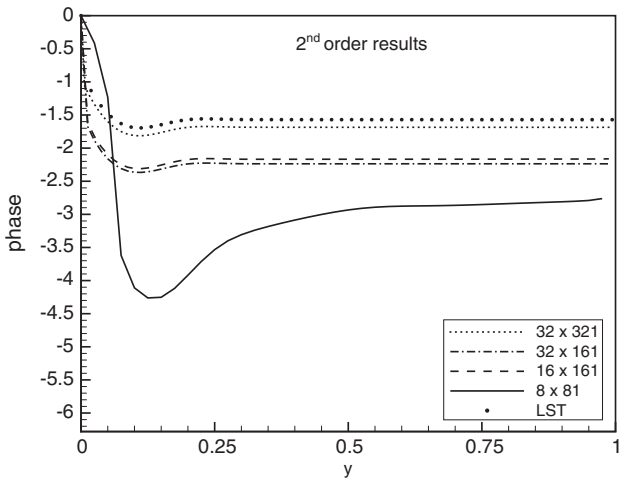

Figure 10. Phase results with different mesh sizes for second-order approximations at $x = 45.89$.

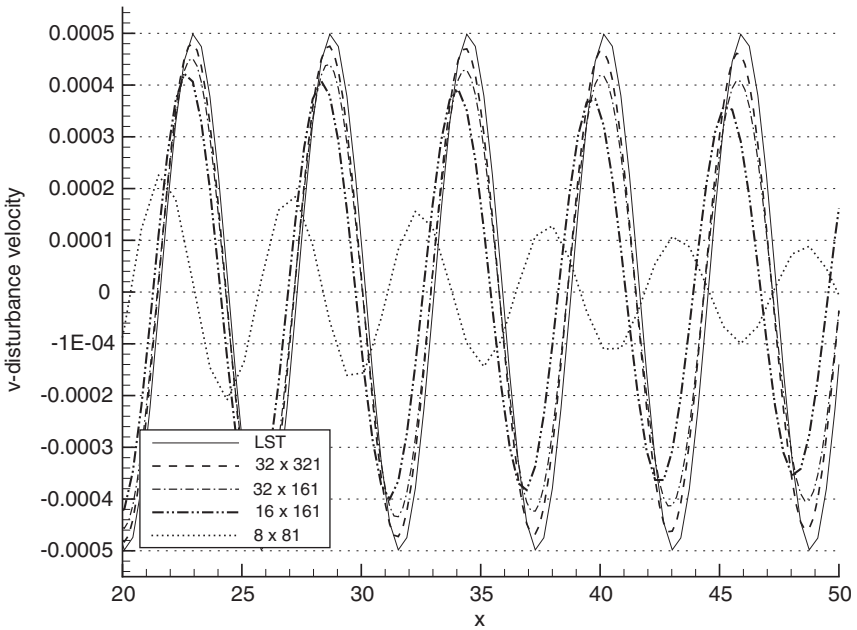

Figure 11. Wall normal velocity component distribution along the streamwise direction, at the centre of the channel.

4.3. Fourth-order explicit approximation results

As one can see in Figure 12, curve 12×121 a, for this scheme, in a mesh using 12×121 grid points, the disturbances were amplified instead of damped with $\alpha_i = -9.88 \times 10^{-5}$. While

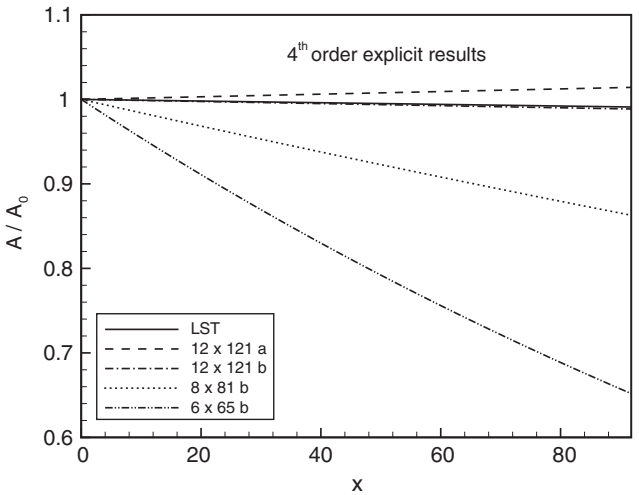

Figure 12. Fourth-order explicit approximations—amplification results.

investigating the possible reasons for this numerical instability, it was found that replacing the fourth-order non-centred approximation, for points next to the boundary ($i = 2$ and $N - 1$), for the second derivative by a non-centred third-order approximation, the instability was eliminated. It can be observed in the Fourier analysis of the difference schemes, given by Figures 3 and 4, that the third-order approximation is more suitable for this kind of study. The results of the simulations are shown in Figure 12—12×121 b. Using 12 points per Tollmien–Schlichting wavelength and 121 points in the wall normal direction the results obtained were in good agreement with the LST. The computing time of this simulation was 237.54 s. In the same figure the results of other simulations with different number of grid points per Tollmien–Schlichting wavelength and in the wall normal direction are plotted. Again, lowering the number of grid points results in a strong amplitude decay.

Figure 13 shows the wall normal phase distribution of the streamwise disturbance velocity component in the wall normal direction. The results obtained with 12×121 grid points were in good agreement with the LST. Reducing the number of grid points results in a dispersion error. By comparing Figure 8 with Figure 13, one finds that the phase distribution obtained with 8×81 mesh with this approximations was worse than the result obtained with 6×65 mesh using sixth-order compact approximations.

4.4. Fourth-order compact approximation results

As shown in Figure 14, the results obtained with this scheme were accurate with as little as 8 points per Tollmien–Schlichting wavelength. This result was obtained using 121 points in the wall normal direction. The computing time for this simulation was 129.48 s. As shown in Figure 14, lowering the number of grid points in the wall normal direction to 81 introduced dissipation in the solution. However, no dispersion error was introduced, as one can see in Figure 15. In this figure one can observe that the dispersion error was comparatively small, even for a coarse grid (6×65), although with a greater dissipation.

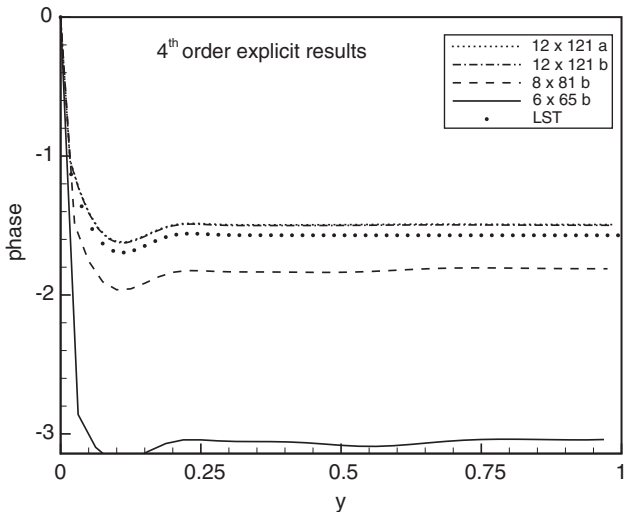

Figure 13. Phase results with different mesh sizes for fourth-order explicit schemes at $x = 45.89$.

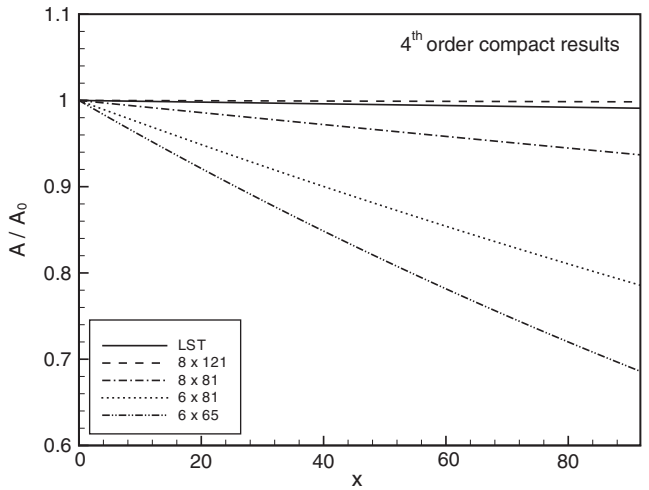

Figure 14. Fourth-order compact approximations—amplification results.

The main advantage of this scheme, when compared with the results obtained with fourth-order explicit scheme was that less points per Tollmien–Schlichting wavelength were needed to capture the correct phase.

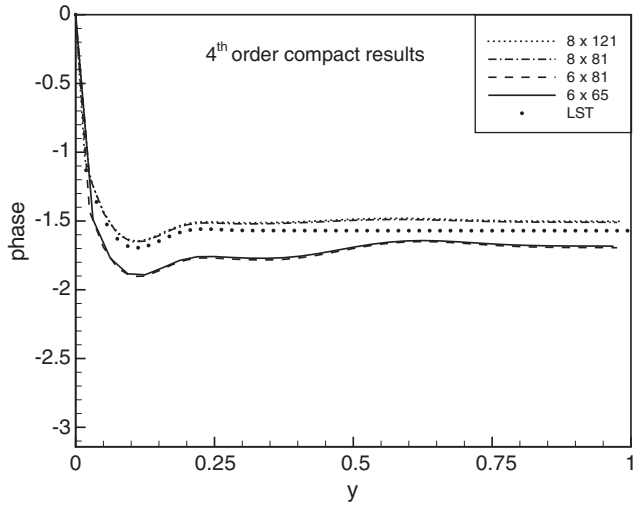

Figure 15. Phase results with different mesh sizes for fourth-order compact schemes at $x = 45.89$.

5. CONCLUSIONS

In this paper, the influence of the spatial discretization scheme on the evolution of stability waves was investigated. The second-order approximation was too dissipative and the grid refinement required to obtain reliable results makes this method exceedingly expensive for these kind of study. The time simulation with the finest grid tested with this method took almost 200 times the effort of the coarsest grid using sixth-order compact approximations, and the solution obtained was not nearly as good.

For the fourth-order explicit approximation, one can observe that the number of points required per Tollmien–Schlichting wavelength was greater than that with the fourth-order compact approximation. It was observed that non-centred approximations near the boundary for the second derivative can introduce numerical amplification in the simulation, resulting in a non-physical solution. This has to be checked when implementing an explicit scheme.

The results with the fourth-order compact scheme showed that the required number of points per Tollmien–Schlichting wavelength was greater than the minimum required when using the sixth-order compact approximations for reliable results. The number of points in the wall normal direction required was much greater, 121 for fourth-order compact approximation against 65 for sixth-order compact approximation.

The sixth-order compact scheme showed good agreement with the linear stability theory, even when using a ‘coarse’ grid with 6 points per Tollmien–Schlichting wavelength and 65 points in the wall normal direction.

Both compact schemes showed phase results better than the non-compact ones for the same wavenumber. These methods should be used when studding wave propagation to minimize dispersion errors.

The main conclusion is that using compact high-order difference schemes in numerical studies can reduce computational effort. These methods should be used in transitional and

turbulent flow simulations where a wide range of length and time scales have to be accurately resolved.

ACKNOWLEDGEMENTS

The authors acknowledge the fruitful discussion with Dr Markus Kloker from the University of Stuttgart during the development of the numerical code. The authors also acknowledge the financial support received from FAPESP.

REFERENCES

1. Davies C, Carpenter P. A novel velocity–vorticity formulation of the Navier–Stokes equations with applications to boundary layer disturbance evolution. *Journal of Computational Physics* 2001; **172**:119–165.
2. Joslin RD. Overview of laminar flow control. *Technical Report NASA TP-1998-209705*, National Aeronautics and Space Administration—NASA, 1998.
3. Joslin RD. Aircraft laminar flow control. *Annual Review of Fluid Mechanics* 1998; **30**:1–29.
4. Biringen S, Laurien E. Nonlinear structures of transition in wall-bounded flows. *Applied Numerical Mathematics* 1991; **7**:129–150.
5. Gmelin C, Rist U, Wagner S. Active control of laminar-turbulent transition using instantaneous vorticity signals at the wall. *Physics of Fluids* 2001; **13**(2):513–519.
6. Laurien E, Kleiser L. Numerical simulation of boundary-layer transition and transition control. *Journal of Fluid Mechanics* 1989; **199**:403–440.
7. Spalart PR. Direct numerical study of crossflow instability. *The IUTAM 90 Symposium on Laminar-Turbulent Transition*, Toulouse, France, 1989.
8. Zang TA, Krist SE, Hussaini MY. Resolution requirements for numerical simulations of transition. *Journal of Scientific Computing* 1989; **4**:197–217.
9. Lele S. Compact finite difference schemes with spectral-like resolution. *Journal of Computational Physics* 1992; **103**:16–42.
10. Mahesh K. A family of high order finite difference schemes with good spectral resolution. *Journal of Computational Physics* 1998; **145**:332–358.
11. Hirsh RS. High order accurate difference solutions of fluid mechanics problems by a compact difference technique. *Journal of Computational Physics* 1975; **19**:90–109.
12. Adam Y. Highly accurate compact methods and boundary conditions. *Journal of Computational Physics* 1977; **24**:10–22.
13. Kloker M. A robust high-resolution split-type compact FD scheme for spatial direct numerical simulation of boundary-layer transition. *Applied Scientific Research* 1998; **59**:353–377.
14. Messing R, Kloker M, Wagner S. Effect of suction through arrays of holes on a 3-d boundary layer investigated by spatial direct numerical simulation. *The IUTAM 99 Symposium on Laminar-Turbulent Transition*, Arizona, U.S.A., 1999.
15. Wassermann P, Kloker M. Direct numerical simulation of the development and control of boundary-layer crossflow vortices. In *New Results in Numerical and Experimental Fluid Dynamics*, Nilsche W, Hilbig R (eds). Berlin, 1998.
16. Wassermann P, Kloker M. Mechanisms and passive control of crossflow-vortex-induced transition in a 3-d boundary layer. *Journal of Fluid Mechanics* 2002; **456**:49–84.
17. Zhang H, Fasel H. Spatial direct numerical simulation of Görtler vortices. *AIAA Fluid Dynamics Conference*, Norfolk, U.S.A., 1999.
18. Ferziger JH, Peric M. *Computational Methods for Fluid Dynamics*. Springer: Berlin, 1997.
19. Fasel H. Untersuchungen zum Problem des Grenzschichtumschlages Durch Numerische Integration der Navier–Stokes-Gleichungen. *Dissertation*, Universität Stuttgart, 1974.
20. Drazin PG, Reid WH. *Hydrodynamic Stability*. Cambridge University Press: Cambridge, 1981.

